Microporous and Mesoporous Materials 236 (2016) 218–227

Contents lists available at ScienceDirect

Microporous and Mesoporous Materials

journal homepage: www.elsevier.com/locate/micromeso

Improved stability in SBA-15 mesoporous materials as catalysts for photo-degradation processes

Verónica R. Elías [a, 1], Gabriel O. Ferrero [a, 1], Rafael G. Oliveira [b], Griselda A. Eimer [a, *]

[a] CITeQ-CONICET Universidad Tecnológica Nacional, Facultad Regional Córdoba, Maestro López esq. Cruz Roja Argentina, 5016, Córdoba, Argentina
[b] CIQUIBIC-CONICET-Universidad Nacional de Córdoba, Facultad de Ciencias Químicas, Argentina

ARTICLE INFO

Article history:
Received 21 June 2016
Received in revised form
31 August 2016
Accepted 1 September 2016
Available online 3 September 2016

Keywords:
Nanostructures
Stability
Metallic species
Catalytic properties

ABSTRACT

SBA-15 materials were modified with Cr, Ni and Fe and characterized by ICP, SAXS, XRD, N_2 adsorption, TPR and UV–Vis DRS. Their photo-catalytic activity was evaluated for the degradation of Acid Orange 7 (AO7) in aqueous suspensions irradiated by artificial UV–Vis light. The results showed that the Cr-modified catalyst exhibited the highest activity. The presence of Cr^{6+} highly dispersed on the internal surface of the SBA-15 structure would be responsible for this observed behavior. Then, when TiO_2 was loaded on this solid, the photo-activity was increased due to a heterojunction effect between the two metals. Moreover, the TiO_2 cover resulted in the Cr species protection leading to a notable decrease of the Cr leaching into the reaction medium. In addition, comparing with the already reported results for modified MCM-41 catalysts, the solid synthesized here allowed achieving the solution biodegradability in shorter irradiation periods and could be re-used even after four cycles without loss of activity. Thus, the high performance of this material leads to make it a very promising photo-catalyst for pre-treatment of recalcitrant contaminants present in aqueous effluents.

1. Introduction

In the last years, photo-catalytic processes on semiconductor surfaces have been the focus of the scientific community interest, particularly due to their applicability in the waste-water treatment. It is known that the photo-catalytic activity is related to the particle size of the semiconductor [1–4]. In this sense, particles of small size, show high surfaces that allow having a high number of photo-catalytic sites. However, when the particles are too small, there are serious difficulties in the recovery of the catalyst from the liquid effluent. Then, a possible solution for this problem has been proposed by means of dispersing photo-catalytic metallic species on mesoporous molecular sieves [5–9]. Among the several structures known up to date, the silica structure SBA-15 emerges as a very attractive material for its high thermal and hydrothermal stability due to its large wall-thickness [10]. Moreover, SBA-15 structures could result appropriate supports, due to other characteristics as inactivity, ordering of long range in the pore arrangement and high surfaces that allow their modification in order to confer different catalytic activities to the final solids. For its part, the most studied semiconductors as TiO_2, SnO_2, ZnO and WO_3 have been identified as potential photo-catalysts for the treatment of organic contaminants as herbicides or synthetic dyes [11–14]. Nonetheless, these semiconductor nanoparticles require the UV-A radiation (320–400 nm) to generate the holes and electrons needed for the photo-catalytic process. Then, when the loaded metallic species on mesoporous supports can absorb low energy radiation, the two major limitations of the current photocatalytic processes could be overcome: the use of artificial UV light of short wavelengths and the difficult recovery of the catalyst from the effluent. In previous reports [15,16], molecular sieves with MCM-41 structure were modified with different transition metals, showing a good performance in the azo-dyes photodegradation. Nevertheless, these molecular sieves must be synthesized from ionic templates and the obtained structures with thinner walls resulted not stable enough to be re-used after several cycles. Then, considering that the SBA-15 structures are synthesized from non-ionic templates and show thicker wall thickness, usually are more stable than the MCM-41 structures. In this sense Das et al. [17] reported the synthesis of Ti-SBA-15 solids which present a good performance as photocatalyst for the degradation of the cationic dye Methylene Blue. Thus, the scope of the present work is to study the photo-activity of SBA-15 modified

* Corresponding author.
E-mail address: geimer@frc.utn.edu.ar (G.A. Eimer).
[1] These authors contributed equally to this article.

http://dx.doi.org/10.1016/j.micromeso.2016.09.001
1387-1811/

with several transition metals (Cr, Ni, Fe) on the azo-dye degradation under UV–Vis light in order to extend the use range of the radiation toward the visible region. The Acid Orange 7 (AO7) was chosen as a dye probe molecule and the obtained results were compared with those already reported for MCM-41 modified with transition metals.

2. Experimental procedures

2.1. Synthesis

The metal-free mesoporous molecular sieve SBA-15 was synthesized as previously reported by Zhao et al. [18]. In a typical synthesis, 4 g of Pluronic P123 (Sigma 99%) used as the structure-directing agent, were dissolved in 30 g of water and 120 g of 2 M HCl solution under stirring at 35 °C. Then, 8.5 g of tetraethoxysilane (TEOS) (Aldrich 98%), the silicon source, was added to that solution and kept under stirring at 35 °C for 20 h. The mixture was aged at 80 °C overnight without stirring. The solid product was recovered, washed and dried at 60 °C. In order to remove the organic template, the solid was submitted to a calcination process at 500 °C for 8 h.

The calcined SBA-15 host was modified with transition metals by the wet impregnation method using aqueous solutions of the corresponding metal precursor [$Cr(NO_3)_3 \cdot 9H_2O$ (Anedra 98%), $Ni(NO_3)_2 \cdot 6H_2O$] (Riedel-de Haën 98%) or $Fe(NO_3)_3 \cdot 9H_2O$ (Aldrich 98%)] in order to reach a theoretical loading of 2.5 wt%. The pH of these impregnation solutions was ~5. In a typical synthesis, 0.75 g of the SBA-15 solid was dispersed in the precursor solution at room temperature and then, the solvent (water) was slowly removed by rotary evaporation at 50 °C for 30 min. The resulting powder was dried at 60 °C and calcined for 8 h at 500 °C. The materials were named: TM/SBA-15(2.5), where TM indicates the loaded transition metal (Cr, Ni or Fe) and in parentheses were indicated the theoretical metal loading. Then, 0.75 g of the more active solid was dispersed in a 3.2 wt% solution of titanium n-butoxide (Fluka 97%) in isopropanol (Cicarelli 99.5%) in order to evaluate some synergistic effect between the metal species that can enhance the photocatalytic activity. This sample was named: TiO_2/TM/SBA-15(2.5).

2.2. Characterization

The SAXS analysis was carried out at the SAXS-1 beamline at the Brazilian Synchrotron Light Laboratory (LNLS) at Campinas, Brazil. The detector was a Pilatus 300k from Dectris. Typical accumulation times were 1–10 s, the sample-detector distances were between 80 and 95 cm, and the wavelength was 1.55 Å. The empty Kapton cell was measured and subtracted from the signals after normalization. Data was radially integrated by using FIT2D V 12.077 from Andy Hammersley at ESRF. Similar results were found using the SAXS-2 beamline at LNLS. Powder X-ray diffraction patterns (XRD) of the samples were recorded in a PANalytical X'Pert Pro diffractometer with Cu Kα radiation ($\lambda = 1.5418$ Å) in the range of 2θ from 20° to 80°. SEM micrographs were obtained in a JEOL model JSM 6380 LV. Gold coverage was applied to make samples conductive. The acceleration voltage was 20 kV. TEM images were obtained in a JEOL Model JEM-1200 EXII System, working voltage: 120 kV. A small drop of the dispersion (sample in water-ethanol 50% solution) was deposited on copper grid and then evaporated in air at room temperature. UV–Vis diffuse reflectance spectra (UV–Vis DRS) in absorbance mode were recorded using a Jasco 650 spectrometer with an integrating sphere in the wavelength range of 200–900 nm. The Cr, Ni and Fe content was determined by Inductively Coupled Plasma Atomic Emission Spectroscopy (ICP) using a spectrophotometer VISTA-MPX CCD Simultaneous ICP-OES-VARIAN. The specific surface was determined using a Micromeritics Pulse Chemisorb 2700. Samples were previously dried using a N_2 flux for 3 h at 350 °C. The specific surface was determined by the Brunauer-Emmett-Teller (BET) method. For some samples, taken as representatives, measurements of N_2 adsorption/desorption isotherms were made in a Micromeritics TriStar II 3020 V1.03 (V1.03). The reducibility of the calcined catalyst was measured by Temperature-Programmed Reduction (TPR) experiments in the Micromeritic ChemiSorb 2720 Instruments. In these experiments, the samples were heated from 298 to 1073 K at a rate of 10 K/min in the presence of 5% H_2/N_2 gas mixture (20 mL/min STP), and the reduction reaction was monitored by the H_2 consumption with a built-in thermal conductivity detector (TCD).

2.3. Catalytic experiments

The degradation experiments were performed with a photoreactor presented schematically in Fig. 1, which consisted of a borosilicate glass tube of 0.85 L capacity with a sintered glass piece placed at the bottom and four UV–Vis lamps (Actinic BL 20 W, Philips) placed around the tube. These lamps emit a continuum spectrum in the wavelength range between 350 and 400 nm and two bands at 404 and 438 nm (above 380 nm correspond to the visible region). These lamps emit mainly in the UV-A range, thus they were chosen to evaluate the activity of the solids under radiation of longer wavelengths than that frequently used in photocatalytic experiments [19]. To avoid the radiation scattering, an aluminum foil was placed around the photo-reactor. For temperature control, a tube was placed in the center of the reactor allowing the circulation of refrigeration water. A circulation pump and a thermostated water bath (20 ± 0.2 °C) were used for this purpose. The suspension volume employed in all of the experiments was 0.5 L with an initial concentration of the AO7 (Aldrich >85%) and the catalyst of 20 ppm (57 μM) and 1 g/L, respectively. Prior to each reaction, the catalyst was calcined at 500 °C. The suspended catalyst in aqueous system was oxygenated using an air flow of 1 L/min, which allowed reach a percentage of oxygen saturation of around 90%. The measured pH of the suspension was 5 and this value was maintained during the process. Prior to irradiation, the suspension was stirred in the dark under air flow for 45 min in order to reach the adsorption/desorption equilibrium. After the adsorption period, an initial sample was extracted to calculate the initial concentration

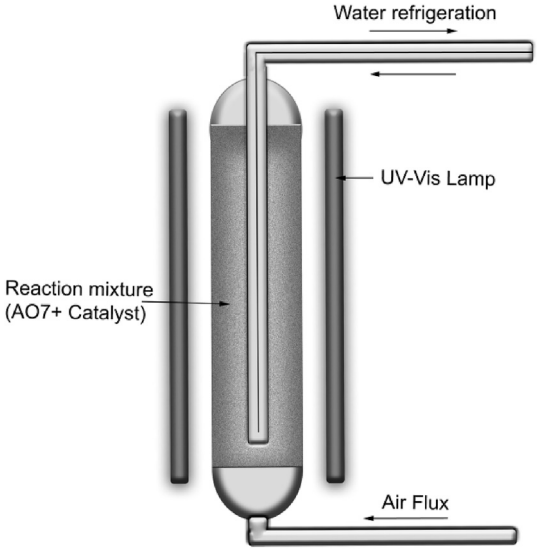

Fig. 1. Reactor scheme.

(C_0) and then, the experimental run starts. Samples were collected each 1 h and filtered. The concentration (C) of AO7 was monitored by measuring the absorbance at λ of 485 nm using Jasco 7800 spectrophotometer. The degradation percentage was calculated as

$$X = \frac{(C_0 - C)100}{C_0} \quad (1)$$

The mineralization degree of AO7 was measured from the Total Organic Carbon (TOC) concentration changes using a TOC Analyzer Schimadzu 5050. The mineralization efficiency was defined by the following equation:

$$TOC_0 = \frac{(TOC_0 - TOC)100}{TOC_0} \quad (2)$$

where TOC is the value of TOC obtained at time t and TOC_0 correspond to the initial value of TOC. In order to evaluate the stability of the more active catalyst in the photodegradation process, this solid was recovered from the reaction suspension after each catalytic cycle, calcined at 500 °C in order to remove the organic molecules that could be adsorbed in the solid surface and again evaluated. In this work the solid was evaluated after 4 catalytic cycles.

The chemical oxygen demand (COD) measurements were obtained by following the closed reflux, colorimetric method [19]. The 5-days biochemical oxygen demand assay (BOD_5) was employed to evaluate changes in the biodegradability of the samples, employing the respirometric method [20].

Table 1
Chemical composition and structural properties of the calcined materials.

Samples	Ti[a] (wt%)	Cr[a] (wt%)	Ni[a] (wt%)	Fe[a] (wt%)	Area[b] (m^2/g)	Band gap energy (eV)
SBA-15	–	–	–	–	794	–
Cr/SBA-15(2.5)	–	2.033	–	–	661	1.29
Fe/SBA -15(2.5)	–	–	–	1.993	631	1.23
Ni/SBA-15(2.5)	–	–	2.131	–	644	2.43
TiO_2/SBA-15	12.733	–	–	–	495	3.04
TiO_2/Cr/SBA-15(2.5)	12.320	1.08	–	–	436	1.87

[a] Determined by ICP-OES.
[b] Determined by BET.

3. Results and discussion

Table 1 summarizes the chemical composition and structural properties of the calcined catalysts. As it can be seen, the specific surface of SBA-15 slightly decreased (~15%) after the metal loading (Cr, Ni or Fe). For its part, structural characterization of mesoporous silica materials has been explored by SAXS in order to identify the ordering of pores. In this analysis the scattering vector q is employed and can be related to the diffraction angle (θ) by using the Bragg equation:

$$\lambda = 2\, d\, \theta \quad (3)$$

in order to obtain:

$$q = 4\pi \frac{\sin\theta}{\lambda} \quad (4)$$

where λ *is* 1.5418 Å. The corresponding spectra of TM/SBA-15(2.5) samples are shown in Fig. 2, where all of the curves present three peaks that can be indexed to the (100), (110), and (200) planes. These peaks evidence the presence of a hexagonal symmetry of long range for the pores, indicating that the structural regularity of the support was remained even after the impregnation with the metallic species and the application of the calcination process. The XRD patterns at high angle (Fig. 2B) show no peaks assignable to the presence of metal oxide phase. Nevertheless, oxide species of very small particle size (lower than the limit detection for XRD technique) could exist and their presence cannot be discarded.

TEM images presented in Fig. 3 give consistent evidence that the structure is preserved in the modified SBA-15 synthesized in this work. In these images, the well-ordered parallel nanotubular pores, characteristic of the hexagonal arrangement, could be clearly observed for SBA-15 and Cr/SBA-15(2.5) samples, where views along the long axis are shown. These images can be taken when the electron beam is perpendicular to the main axis of the cylindrical

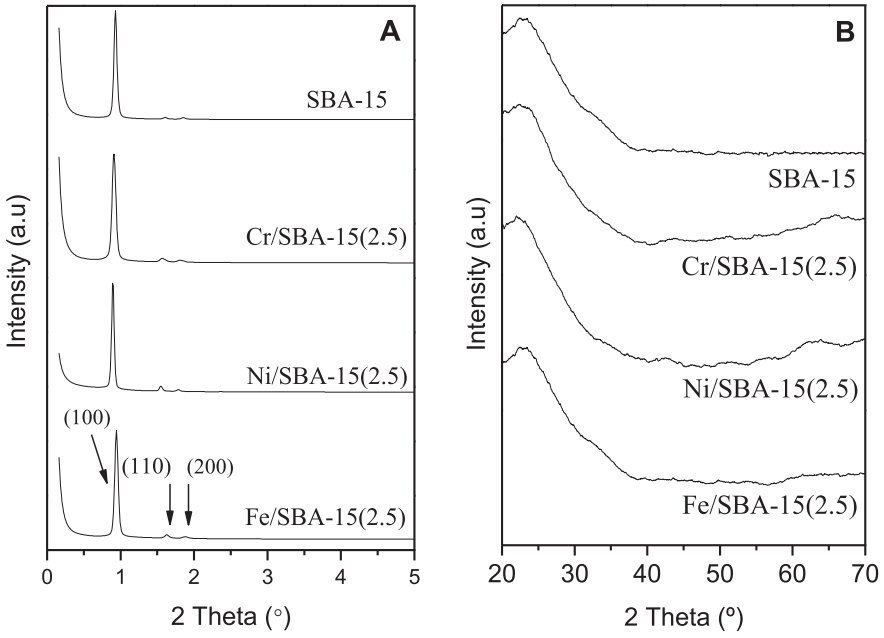

Fig. 2. SAXS and XRD patterns at high angle of the synthetized samples.

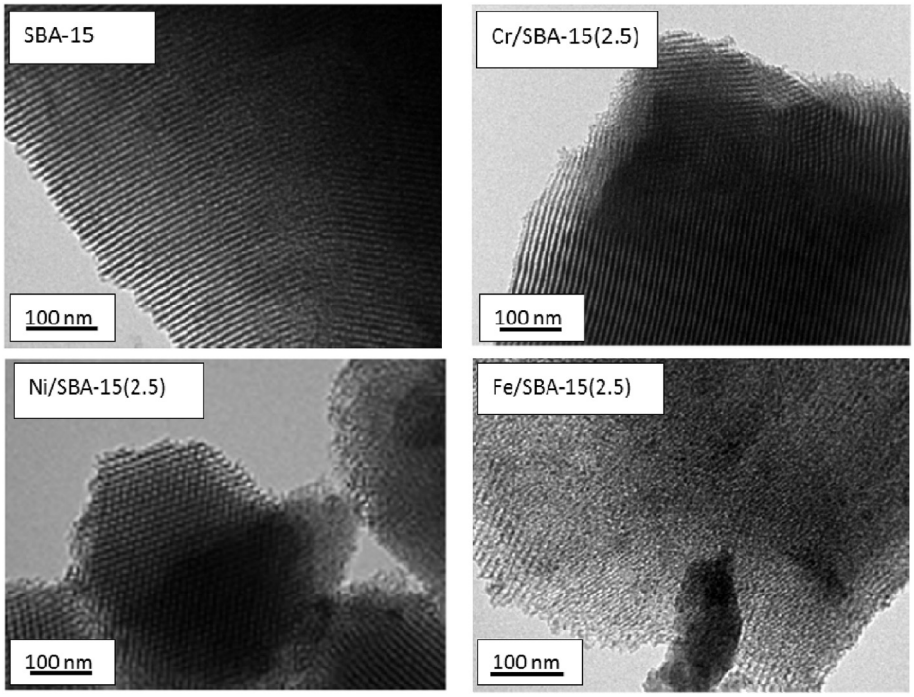

Fig. 3. TEM images of the synthetized materials.

pores. In change, when the electron beam is parallel to pore axis, frontal views of them could be observed giving account for the good structure of the obtained solids. This kind of views were observed for Cr/SBA-15(2.5), Fe/SBA-15(2.5) and particularly for the Ni/SBA-15(2.5) samples. In these TEM images it is shown that the regular hexagonal array of uniform channels in which each pore is surrounded by six neighbors is retained and unaffected by the presence of metals. In this way, by means of TEM, it could be confirmed that the introduction of metal species does not alter the regular order array of mesopores. In addition the average pore diameter for all of the samples was of around 7.2 nm. Finally, the places with darker contrast can be ascribed to the presence of metal oxide nanoparticles which are located inside the channels of SBA-15 and that became into small crystallites after the calcination process [21]. Moreover, no bigger oxide particles segregated in the external surface of the solids were observed by TEM. Scanning electron microscopy (SEM) images of some of the samples are shown in Fig. 4. Here, it could be observed that the bare SBA-15 and the solids

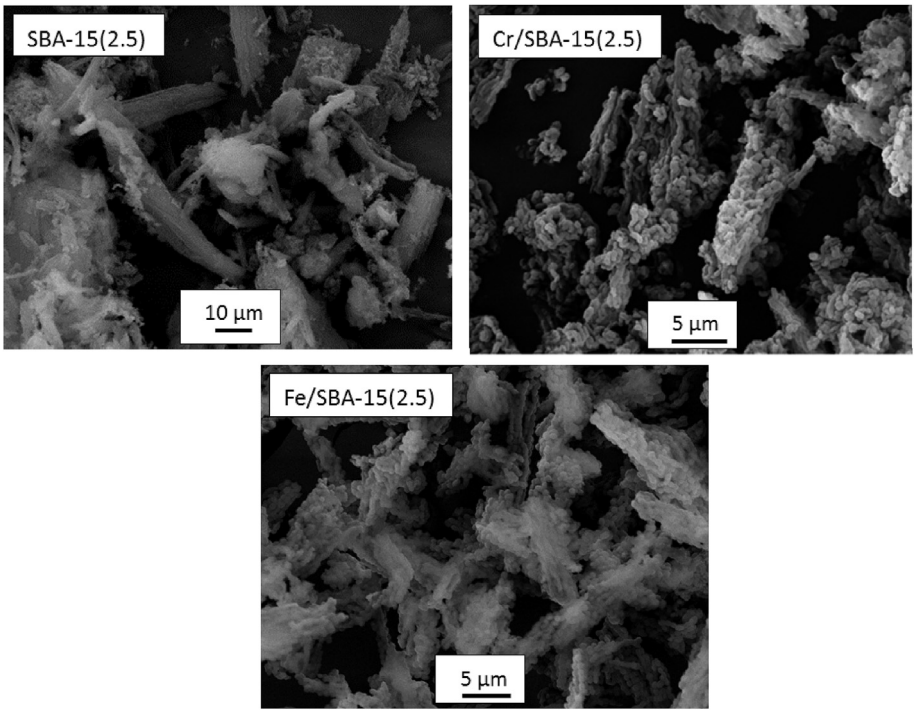

Fig. 4. SEM images of the synthetized materials.

modified with a metal loading of 2.5 wt% show similar morphologies. In the pictures, the presence of bigger size agglomerates suggests the confluence and aggregation of primary small particles that form micron-sized aggregates. Some fibrous type morphologies which are common in the SBA-15 type materials were also observed. This type of morphology has been proven to have long channels with the 2D-hexagonal structure directions parallel to the long axis [22].

Considering that the SAXS, TEM and SEM analyses of the solids indicate the similarity in the structure for samples modified with a 2.5 wt%, the Fe/SBA-15(2.5) sample was be taken as representative for all these materials. Then, this isotherm and the one corresponding to the pure SBA-15 are shown in Fig. 5. As it can be observed the isotherms are classified as IV type according to IUPAC and are reversible up to 0.6/0.7 of relative pressure. In addition, they show H1 hysteresis loops, usually found in mesoporous materials. According to Barrera et al. [23] this kind of isotherms indicates that adsorption at low relative pressure is due to filling of micropores or a strong adsorbate/adsorbent interaction, while at higher pressures may be attributed to mono-/multi-layer adsorption of N_2 on mesopore walls. The capillary condensation (adsorption branch) on the primary mesopores occurred at relative pressures of around 0.7, with a pronounced inflection indicating a narrow and uniform pore size distribution, which is in good agreement with TEM results. For its part, the adsorption and desorption branches in the hysteresis loops were parallel, being typical of materials with cylindrical geometries and uniform pore sizes. In the case of the sample modified with metal, the decrease in the slope at P/P_0 around 0.8 could be the result of the decrease in the external surface, which may be related to an improved alignment of the cylinders indicating the better structural order.

Fig. 6 shows the UV–Vis spectra of the pure SBA-15 and the TM/SBA-15(2.5) samples. For pure SBA-15, there were two very weak bands at around 250 and 310 nm which could be due to charge transfer characteristics of UV absorption of the SBA-15 skeleton, since no metal is present in this material. After Cr loading, four absorption bands at around 260, 359, 457 and 600 nm were detected. As it was already descripted in a previous report [16], the location of the former three bands indicates the presence of (Cr^{6+}) in monochromate and di/poly-chromate species, whereas the last band is a result of d–d transitions of Cr^{3+} probably present in clusters and nanoparticles of α-Cr_2O_3 [24–31]. Contrary to the already reported on Cr/MCM-41 samples with low metal loadings, where in the UV–Vis spectra [16] only bands corresponding to oxidized Cr species appeared, the spectrum of sample synthesized

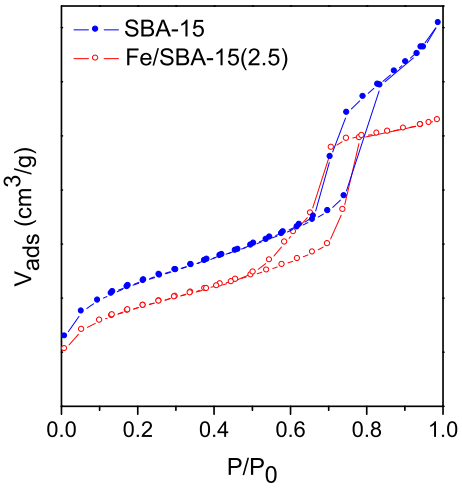

Fig. 5. N_2 adsorption/desorption isotherms of samples taken as representatives.

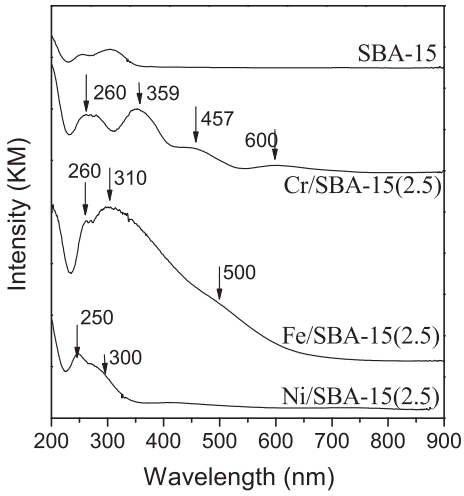

Fig. 6. UV–Vis DR spectra of the synthetized TM/SBA-15(2.5) samples.

here showed the presence of Cr^{3+} species even for the low Cr content evaluated. It is known that after the calcination process, oxidized Cr species are formed in the surface. Nevertheless, the Cr can be stabilized in the hexavalent state until the saturation coverage of the support surface is reached. Beyond this limit, Cr^{3+} species are formed. Here, the lower areas of SBA-15 structures (794 m^2/g), in comparison to those of MCM-41 (1182 m^2/g), probably lead to the beginning of the surface saturation even at low Cr concentration. Thus, the calcination process could not completely oxidize the Cr species resulting in the formation of clusters and nanoparticles of Cr_2O_3. Nevertheless, the relative intensity of the observed bands indicates the majority presence of Cr^{6+} species in mono and di/polychromate on Cr/SBA-15(2.5) sample, with a minimum presence of octahedral Cr^{3+} (in clusters and nanoparticles of Cr_2O_3). Then, when the mesoporous silicate was modified with Ni, the absorption at around 250–350 nm is associated to the $O^{2-}(2p) \rightarrow Ni^{2+}(3d)$ charge transfer of octahedral Ni^{2+} species in NiO lattices [32,33]. Nonetheless, the absorption at 250 nm could also be assigned to the presence of isolated Ni^{2+} that cannot be discarded. In addition, the absorption at wavelengths higher than 400 nm is associated to d–d transitions of Ni^{2+} ions in octahedral local environment indicating the presence of NiO in clusters or nanoparticles. Comparing with the results obtained for Ni/MCM-41 solids [34], the presence of this oxide phase in the Ni/SBA-15(2.5) modified with a low loading of metal, again, evidences the lower saturation limit of the surface in these structures. Meanwhile, the spectrum corresponding to the Fe/SBA-15(2.5) sample shows absorptions at 260 and 310 nm. The former band has been assigned to $t_1 \rightarrow t_2$ and $t_1 \rightarrow e$ transitions involving Fe^{3+} in tetrahedral coordination $[FeO_4]^-$. Meanwhile, the band at higher wavelengths indicates an octahedral coordination of Fe^{3+} probably in small clusters $(FeO)_n$ [35]. Finally, the absence of an absorption band centered at 500 nm indicates that, for the tested metal loading, aggregated iron oxide clusters of bigger size or oxide nanoparticles were not formed [15].

On the other hand, the band-gap energy (Eg) of the photocatalysts were calculated from the UV–Vis DR spectra and summarized in Table 1. These were determined from the following Kubelka-Munk (K-M) equation:

$$F(R) = \frac{(1-R)^2}{2R} \quad (5)$$

where R is the reflectance (%) and F(R) is a proportional of the extinction coefficient. By plotting the K-M as a function of the

energy (eV), the Eg value for each solid could be determined following the Tauc method [36]. It is worth to note that these values are deeply dependent on composition and size of the oxide species loaded in the silica matrix due to the resulting quantic effects [37]. The sample only modified with TiO_2 present the higher Eg values, which is indicating that it could be activated only with high energy radiation. Meanwhile, samples modified with transition metal have the following Eg: 2.43, 1.29, 1.23 and 1.89 eV for samples Ni/SBA-15(2.5), Cr/SBA-15(2.5), Fe/SBA-15(2.5) and TiO_2/Cr/SBA-15(2.5), respectively. These values are indicating that samples modified with Ni, Cr and Fe could be active under lower energy radiation. Finally, even though all the materials modified with TM show lower Eg values, it is necessary to consider that this fact is a necessary condition for their photoactivity under low energy radiation (shifted to the visible range), but it is not sufficient to perform as an efficient photocatalyst.

The UV–Vis DR results were confirmed by TPR measurements which are generally useful as a fingerprint of the TM species interacting with the support silicate. The TPR profiles of the synthetized samples are shown in Fig. 7. In the case of the Fe/SBA-15(2.5) sample, two hydrogen consumptions appear at 372 and 590 °C. These can be related to $Fe_2O_3 \rightarrow Fe_3O_4$ and $Fe_3O_4 \rightarrow FeO$ processes, respectively. However, the first consumption is higher than the second, indicating that the Fe^{3+} species are mainly reduced only to Fe^{2+} species, which are stabilized in the SBA-15 structure with high resistance to the reduction to metallic state [38,39]. For its part, the Ni/SBA-15(2.5) TPR profile contains a main peak with a maximum at 397 °C that can be attributed to octahedral Ni(II) species already detected by UV–Vis DR analysis. In fact, this consumption is characteristic of bulk NiO usually formed when the wet impregnation method is used to load Ni on molecular sieves. Nevertheless, the small shoulder at higher temperatures (around 550 °C) has already been assigned to the presence of isolated Ni ions, whose presence could not be discarded [40,41]. With respect to the Cr/SBA-15(2.5) sample, one single small reduction band at around 465 °C, due to the reduction of Cr^{6+} to Cr^{3+} ions was observed. The presence of only one reduction temperature would be giving account for the predominance of Cr^{6+} species as monochromates of high interaction with the support. This fact would be a consequence of the higher dispersion of these species due to the low Cr content [42–44]. Based on these results we can conclude that in this sample, the Cr mainly exists in 6 + oxidation state as mono and di/polychromates. Then, the TiO_2/Cr/SBA-15(2.5) sample presented only one reduction peak at around 277 °C, which can be attributed to the reduction of Cr^{6+} to Cr^{5+} which would be hardly further reduced due to their covering by the titania, avoiding the reduction to Cr^{3+} [45]. Moreover, it is worth to note that the lower hydrogen consumption of this sample with respect to the Cr/SBA-15(2.5) sample probably is a consequence of the stabilization of the oxidized Cr species in the SBA-15 structure by their covering with TiO_2. Thus the TPR analysis allows us to confirm about the presence of the TM species already observed by UV–Vis DR. Finally the smaller hydrogen consumption observed for all the TM samples, would be consequence of the low TM loading and the shielding effect of the mesoporous framework. Thus, the highly dispersed TM species on the SBA-15 structure are less accessible being protected from H_2 attack avoiding their complete reduction to the zero valence state.

3.1. Photocatalytic evaluation

At first it is important to indicate that the AO7 concentration used in this work was chosen because it is an average value among the concentration found in textile industry effluents [46–50]. For its part, the catalyst concentration was chosen in order to have a sufficient number of active sites without affecting the efficiency of radiation because of an opaque suspension [51]. On the other hand, experiments without catalyst and in the dark were previously carried out. Thus, without the presence of catalyst, no appreciable photo-degradation was observed during 5 h under UV–Vis irradiation (X~10%). Meanwhile, no degradation was observed (X<1%) using the catalyst but in dark. Then, Fig. 8 shows the photo-degradation of AO7 using the synthesized solids under UV–Vis radiation. As it could be observed, Cr/SBA-15(2.5%) was the one with higher activity (72.9%). This behavior is probably due to the more efficient use of the radiation because the next transition: $Cr^{6+}–O^{2-} \rightarrow Cr^{5+}–O^{1-}$ is possible [16]. It was already reported that this charge-transfer excited state has high reactivity due to the presence of electron-hole pairs localized next to each other. Then, these pairs can interact with surface hydroxyl groups on SBA-15 or different adsorbed species to produce radical species that initiate the photo-catalytic degradation. Meanwhile, the poor activity of SBA-15 solids modified with Ni, and particularly with Fe, could be related to that both metals could act as recombination centers that accelerate the electron-hole recombination hindering the photo-activity. However, a small number of photo-catalytic sites are available for the reaction (particularly on the Ni/SBA-15(2.5)) giving account for the activity observed. Nevertheless, when Cr/SBA-15(2.5) is employed as catalyst, 7 ppm of Cr were detected in the final reaction mixture, indicating the lixiviation of the metal from

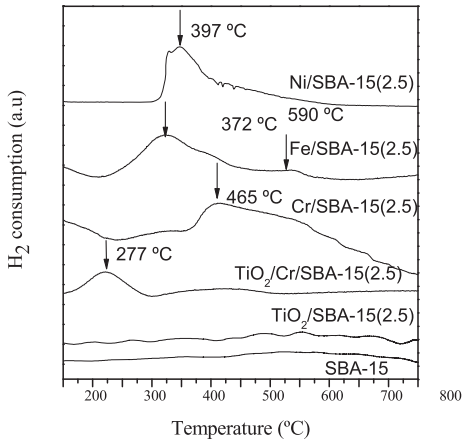

Fig. 7. TPR profiles of the synthetized samples.

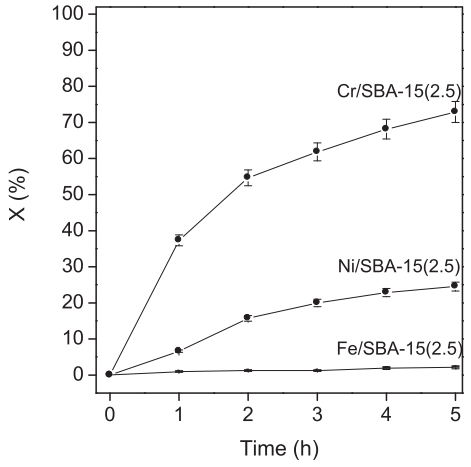

Fig. 8. AO7 degradation using the synthesized TM/SBA-15(2.5).

the siliceous material into the solution. Thus, in order to reduce the Cr lixiviation, the material was further impregnated with a Ti loading of ~20 wt%. For comparative purposes the TiO_2/SBA-15 was also synthesized. These samples were characterized and photocatalytically evaluated (Table 1).

SAXS analysis (Fig. 9) indicated that the presence of TiO_2 has not greatly modified the structural ordering of SBA-15 and Cr/SBA-15(2.5) samples, maintaining the reflections of the planes (100), (110) and (200) which are typical of the hexagonal arrangement of the pores. For its part, the XRD patterns (Fig. 9) show the diffractions at the angles characteristic of TiO_2 in the anatase form [16]. Meanwhile, TEM show the images of the straight mesochannels arraying along the long axis and of the hexagonal arrangement of the unidirectional mesopores, confirming that the highly ordered structure of the SBA-15 support was retained after the loading of both metals [TiO_2/Cr/SBA-15(2.5)] (Fig. 10). Nonetheless, in comparison with metal free SBA-15 sample, the loading with TiO_2 resulted in a notable decrease of the specific surface (around 40%) probably due to the presence of anatase finally dispersed inside the channels as well as segregated on the external surface in the form of bigger size nanoparticles which would be affecting the pore structure.

As it can be observed in Fig. 10, although the regular structure is notable for both samples, some black spot of size bigger than the pore could be observed. These would be confirming the presence of oxide particles segregated in the external surface which would be responsible for the marked decrease in the specific area. Then, in Fig. 11 it could be observed that the fiber type morphology showed for the samples without TiO_2 is preserved. Nevertheless, in these images it is more notorious that this morphology results from the agglomeration of smaller spherical nanoparticles.

For its part, from UV–Vis DR characterization (Fig. 12), it could be observed that the presence of both metals (Ti and Cr) provoked an increase in the absorption in the 350–500 nm range with respect to the TiO_2/SBA-15 spectrum, due to the presence of Cr species. This increase in the absorption in the visible region of the spectra has also been observed in solids MCM-41 modified with Cr and Ti [15,16]. This fact could be associated to a heterojunction effect between the titania and the oxidized Cr species that allows a more efficient use of radiation by using longer wavelength light [24,52,53]. Thereby, TiO_2/Cr/SBA-15(2.5) sample enhanced its ability to absorbing visible light with respect to the TiO_2/SBA-15 (Fig. 12).

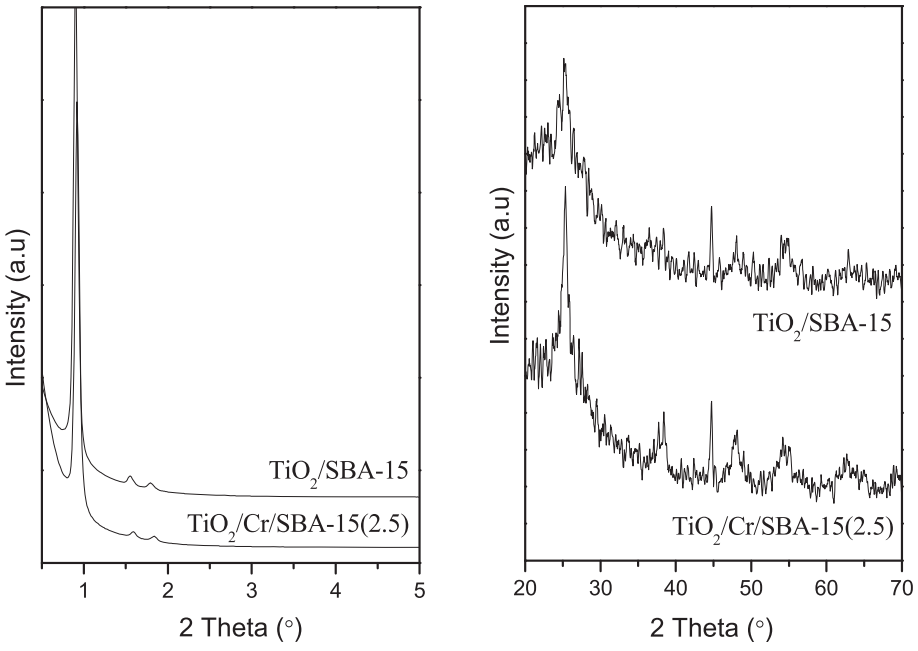

Fig. 9. SAXS and XRD analysis of samples modified with a high load of Ti.

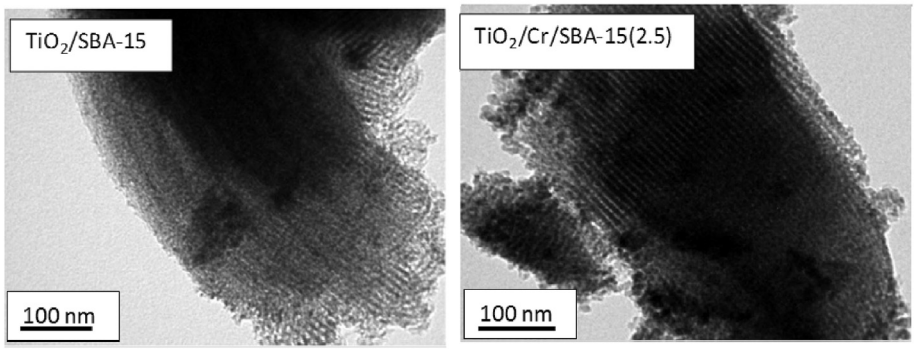

Fig. 10. TEM images of samples modified with a high load of Ti.

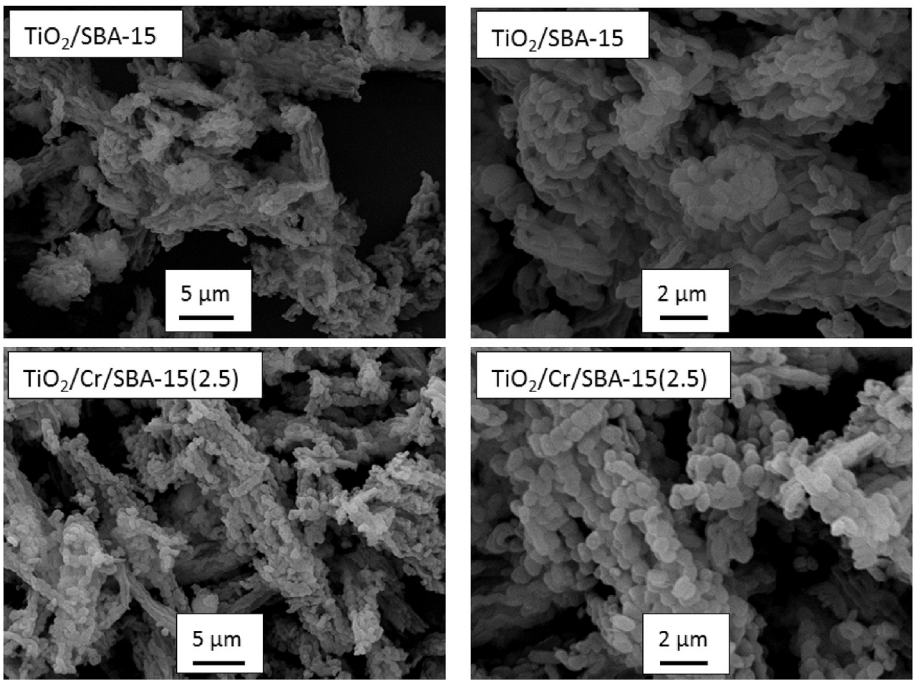

Fig. 11. SEM images of samples modified with a high load of Ti.

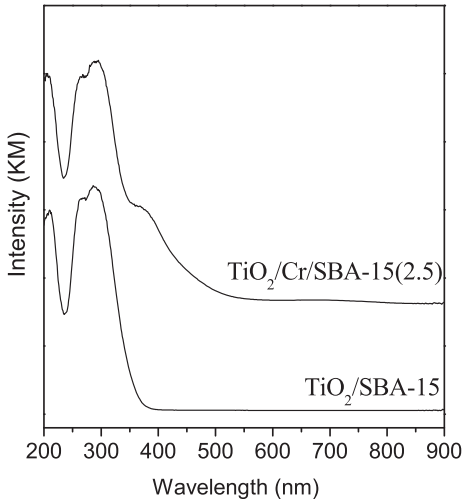

Fig. 12. UV–Vis DR spectra of TiO_2/SBA-15 and TiO_2/Cr/SBA-15(2.5) samples.

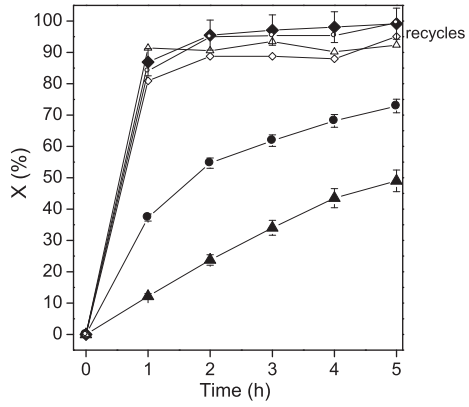

Fig. 13. AO7 degradation using the synthesized of samples: (▲) TiO_2/SBA-15, (●) Cr/SBA-15(2.5), (◆) TiO_2/Cr/SBA-15(2.5) 1st cycle, (□) TiO_2/Cr/SBA-15(2.5) 2nd cycle, (Δ) TiO_2/Cr/SBA-15(2.5) 3rd cycle, (○)TiO_2/Cr/SBA-15(2.5) 4th cycle.

With respect to the photo-catalytic evaluation, Fig. 13 and Table 2 show the AO7 photo-degradation reached after the TiO_2 loading. As it could be observed TiO_2/Cr/SBA-15(2.5) (X ~ 99.2) is more active than Cr/SBA-15(2.5) (X ~ 72.9) and TiO_2/SBA-15 catalysts (X ~ 49.0). This behavior can be due to a sensitization of TiO_2 with the Cr^{6+} species as result of the already mentioned hetero-junction effect (UV–Vis DR analyses) that emerges when both metals were loaded in the silicates. Moreover, the additional activity of Ti itself under UV radiation should be also considered for this sample (activity observed for the TiO_2/SBA-15). Thus, when TiO_2 was loaded on the Cr/SBA-15(2.5) the almost total AO7 degradation is observed. In addition to the high activity found for this solid, the Cr leaching was notably reduced after the TiO_2 loading (to ~ 1 ppm) indicating that the Cr was efficiently retained on the mesoporous surface. This fact is probably consequence of the protection that results from the TiO_2 cover that avoids the Cr lixiviation.

Finally, one of the most important advantages of the heterogeneous catalysts, compared to the homogeneous ones, is that they can be re-used. For this, an essential point that should be considered is the stability of the active component with respect to leaching. Therefore, the nature of the catalysis is a crucial factor in the liquid-phase process and it is very important to evaluate how many times the catalyst maintains its activity under the selected reaction conditions. Despite the high photo-activities in the AO7 degradation already reported for MCM-41 silicates modified with Cr and Ti [16], these solids were not stable enough after several catalytic cycles. Taking into account that the SBA-15 silicates are more stable structures, the recyclability of the most active catalyst, TiO_2/Cr/SBA-15(2.5), was evaluated. In this sense, the solid was

Table 2
X, COD, BOD_5 and biodegradability ratio (BOD_5/COD) reached after 5 h of radiation using the optimized catalyst.

Reaction time (h)	BOD_5 (mg/L O_2)	COD (mg/LO_2)	BOD_5/COD
0	2.0	16.4	0.1
5	5.5	10.3	0.5

BOD_5: Biochemical oxygen demand.
COD: Chemical oxygen demand.

recovered after each run, dried, calcined at 500 °C and re-used in a new catalytic test. The AO7 degradation obtained after each cycle is depicted in Fig. 13, where no obvious loss of activity was observed even after four runs. These experiences demonstrate that the optimized catalyst has two major advantages: very high levels of dye degradation and possibility of catalyst reuse after several catalytic cycles. This excellent solid performance could be consequence of the major stabilization of the oxidized Cr species after the loading with TiO_2. Probably, the higher pore size of the SBA-15 solid (~7 nm), in comparison with that of the MCM-41 structures (~3.5 nm), allows the easier diffusion of Ti species toward the pores. Then, the covering of the Cr species is improved and their stabilization on the surface is enhanced. Contrary, when the pore diameter is small (for MCM-41 structures) the diffusion of Ti species is more difficult and some Cr species, that could not be adequately protected, lixiviate from the surface during the consecutives catalytic cycles, provoking the loss in the activity. On the other hand, is important to remark that after 5 h of radiation using the TiO_2/Cr/SBA-15(2.5) catalyst a mineralization degree of around 30% could be achieved. Fig. 14 shows that after four cycles both values, the AO7 degradation and the mineralization, were kept constant. Therefore, as it can be observed in the Table 2, even although the mineralization was not elevated, the biodegradability of the treated solution was achieved [54–56]. Thus, the BOD_5/COD ratio changed from 0.1 to 0.5 after 5 h of irradiation, when the AO7 degradation was 98.8%. Finally, although the complete mineralization was not reached, the biodegradability could be enhanced by the photocatalytic process converting non-biodegradable organics into their biodegradable forms. Moreover, it is very important to note that the modified SBA-15 allowed reaching the biodegradability in a shorter time than that required by using modified MCM-41 structures as photo-catalysts [57]. Thus, the photocatalytic process presented in this work using TiO_2/Cr/SBA-15(2.5) solid under UV–Vis light emerges as a very promising fast treatment, which could be applied previous to a conventional biological degradation process.

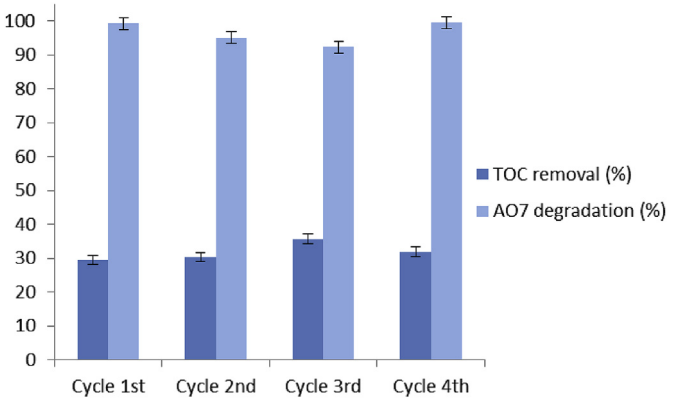

Fig. 14. AO7 photodegradation and mineralization degree as function of cycle number of usage for TiO_2/Cr/SBA-15(2.5) catalyst.

4. Conclusion

SBA-15 molecular sieve with high specific areas, average pore diameter of around 7 nm and long range structural order of pores, could be successfully synthesized and used as support for several transition metal species (Cr, Ni, Fe). All of the modified-materials also exhibited good structural regularity retaining the hexagonal pore arrangement after the metal loading. Among all the evaluated metals, Cr modified SBA-15 showed the higher photo-activity in the azo-dye degradation. Nevertheless, the further loading with TiO_2 enhanced the catalyst performance in two major aspects: 1) increase in the AO7 degradation due to a heterojunction effect between Ti and Cr, resulting in a more efficient use of radiation and 2) a notably decrease of the Cr leaching into the reaction medium. It is important to note that the last aspect also contribute to the catalyst recyclability. In this sense, the solid could be re-used even after four cycles without loss of activity. For its part, even if the complete mineralization was not reached, after applying photo-catalytic process, the biodegradability of the dye solution was achieved in only 5 h of radiation. In fact, the solid synthesized here, from a stable structure as SBA-15, leads to a photocatalyst that shows more stability in comparison with those arising from MCM-41 structures. Finally, the TiO_2/Cr/SBA-15(2.5) silicate of high performance obtained in this work, can be proposed as an efficient catalyst for the pre-treatment of recalcitrant contaminants as azo-dyes, due to its high photo-activity and re-use capacity.

Acknowledgements

V.R.E, G.O.F, R.G.O, S.G.C and G.A.E are members of CONICET. The authors are gratefully to UTN for the financial support. The authors acknowledge beamtime to the Brazilian Synchrotron Light Laboratory (LNLS) at Campinas, Brazil, experimental stations SAXS-1 and SAXS-2. The authors are gratefully to Ph.D Eliana G. Vaschetto for the TEM and SEM images.

References

[1] D. Beydoun, R. Amal, G.K. Low, S. McEvoy, J. Phys. Chem. B 104 (2000) 4387–4396.
[2] H.Y. Zhu, J. Orthman, J.Y. Li, J.C. Zhao, G.J. Churchman, E.F. Vansant, Chem. Mater. 14 (2002) 5037–5044.
[3] X. Zhang, F. Zhang, K.Y. Chan, Appl. Catal. A 284 (2005) 193–198.
[4] W.Y. Jung, B. Ho Noh, S.H. Baek, G.D. Lee, S.S. Park, S.S. Hong, React. Kinet. Catal. Lett. 91 (2007) 223–231.
[5] J. Yang, K. Hidajat, S. Kawi, J. Mater. Chem. 19 (2009) 292–298.
[6] B.J. Aronson, C.F. Blanford, A. Stein, Chem. Mater. 9 (1997) 2842–2851.
[7] M.S. Morey, S. O'Brien, S. Schwarz, G.D. Stucky, Chem. Mater. 12 (2000) 898–911.
[8] S. Zheng, L. Gao, Q.H. Zhang, J.-K. Guo, J. Mater. Chem. 10 (2000) 723–727.
[9] S. Zheng, L. Gao, Q.H. Zhang, W. Zhang, J.K. Guo, J. Mater. Chem. 11 (2001) 578–583.
[10] K.M. McGrath, D.M. Dabbs, N. Yao, I.A. Aksay, S.M. Gruner, Science 277 (1997) 552–556.
[11] M.A. Brown, S.C. de Vito, Crit. Rev. Environ. Sci. Technol. 23 (1993) 249–324.
[12] N.A. Lewis, M.L. Rosenbluth, in: N. Serpone, E. Pelizzetti (Eds.), Photocatalysis Fundamentals and Applications, John Wiley and Sons, New York, 1989, pp. pp.45–98.
[13] A. Mills, R.H. Davies, D. Worsley, Chem. Soc. Rev. 22 (6) (1993) 417–425.
[14] M.R. Hoffmann, S.T. Martin, W. Choi, D.W. Bahnemann, Chem. Rev. 95 (1) (1995) 69–96.
[15] V. Elías, E. Vaschetto, K. Sapag, M. Oliva, S. Casuscelli, G. Eimer, Catal. Today 172 (2011) 58–65.
[16] V. Elías, E. Sabre, K. Sapag, S. Casuscelli, G. Eimer, Appl. Catal. A 413–414 (2012) 280–291.
[17] S. Das, M. Bhunia, A. Bhaumik, J. Solid State Chem. 183 (2010) 1326–1333.
[18] D. Zhao, J. Feng, Q. Huo, N. Melosh, G.H. Fredrickson, B.F. Chmelka, G.D. Stucky, Science 279 (1998) 548–552.
[19] L. Davydov, E.P. Reddy, P. France, P.G. Smirniotis, J. Catal. 203 (2001) 157–167.
[20] Standard Methods for the Examination of Water and Wastewater, twentieth ed., American Public Health Association/America Water Works Association/Water Environmental Federation, Washington DC, 1998.
[21] L. Yu, X. Yang, D. Wang, J. Col. Interf. Sci. 448 (2015) 525–532.

[22] H. Zhang, J. Sun, D. Ma, X. Bao, A. Klein-Hoffmann, G. Weinberg, D.S. Su, R. Scho, J. Am. Chem. Soc. 126 (2004) 7440–7441.
[23] D. Barrera, J. Villarroel-Rocha, L. Marenco, M. Oliva, K. Sapag, Adsorpt. Sci. Technol. 29 (2011) 975–988.
[24] F. Marques, M. Canela, A. Stumbo, Catal. Today 133–135 (2008) 594–599.
[25] S. Shylesh, P. Samuel, A.P. Sing, Appl. Catal. A 318 (2007) 128–136.
[26] M. Anpo, T. Kim, M. Matsuoka, Catal. Today 142 (2009) 114–124.
[27] B. Weckhuysen, I. Wachs, R. Schoonheydt, Chem. Rev. 96 (1996) 3327–3349.
[28] X. Fan, X. Chen, S. Zhu, Z. Li, T. Yu, J. Ye, Z. Zou, J. Mol. Catal. A 284 (2008) 155–160.
[29] D. Beydoun, R. Amal, G. Low, S. McEvoy, J. Nanoparticle Res. 1 (1999) 439–458.
[30] S. Rodrigues, S. Uma, I. Martyanov, K. Klabunde, J. Catal. 230 (2005) 158–165.
[31] Y. Ohishi, T. Kawabata, T. Shishido, K. Takaki, Q. Zhang, Y. Wang, K. Takehira, J. Mol. Catal. A 230 (2005) 49–58.
[32] V. Volkov, Z. Wang, B. Zou, J. Phys. Chem. Lett. 337 (2001) 117–124.
[33] A. Tirsoaga, D. Visinescu, B. Jurca, A. Ianculescu, O. Carp, J. Nanopart. Res. 13 (2011) 6397–6408.
[34] P. Carraro, V. Elías, A. García Blanco, K. Sapag, S. Moreno, M. Oliva, G. Eimer, Microporous Mesoporous Mater. 191 (2014) 103–111.
[35] E. Suzuki, K. Nakashiro, Y. Ono, Chem. Lett. 17 (1988) 953–956.
[36] M. Li, J.C. Li, Mater. Lett. 60 (2006) 2526–2529.
[37] R. López, R. Gómez, J. Sol-Gel Technol. 61 (2012) 1–7.
[38] B. Coq, M. Mauvezin, G. Delahay, S. Kieger, J. Catal. 195 (2000) 298–303.
[39] H. Hayashi, L. Chen, T. Tago, M. Kishida, K. Wakabayashi, Appl. Catal. A 231 (2002) 81–89.
[40] R. Baran, I. Kaminska, A. Srebowata, S. Dzwigaj, Microporous Mesoporous Mater. 169 (2013) 120–127.
[41] T. Jiang, Y. Tang, Q. Zhao, H. Yin, Colloids Surfaces 315 (2008) 299–303.
[42] L. Zhang, Y. Zhao, H. Dai, H. He, C.T. Au, Catal. Today 131 (2008) 42–54.
[43] K. Takehira, Y. Ohishi, T. Shishido, T. Kawabata, K. Takaki, Q. Zhang, Y. Wang, J. Catal. 224 (2004) 404–416.
[44] A. Gaspar, J. Brito, L. Dieguez, J. Mol. Catal. A 203 (2003) 251–266.
[45] I. Dellien, F.M. Hall, L.G. Hepler, Chem. Rev. 76 (1976) 283–310.
[46] M. Stylidi, D. Kondarides, X. Verykios, Appl. Catal. B 47 (2004) 189–201.
[47] C. Bauer, P. Jacques, A. Kalt, J. Photochem. Photobiol. A 140 (2001) 87–92.
[48] J. Monteagudo, A. Durán, Chemosphere 65 (2006) 68–76.
[49] K. Rao, B. Lavédrine, P. Boule, J. Photochem. Photobiol. A 154 (2003) 189–193.
[50] J. Fernández, J. Kiwi, C. Lizama, J. Freer, J. Baeza, H. Mansilla, J. Photochem. Photobiol. A 151 (2002) 213–219.
[51] M. Blesa, B. Sanchez (Eds.), Eliminación de contaminantes por Fotocatálisis Heterogénea, Ciemat, Madrid (, 2004, pp. 305–329.
[52] J.A. Pedraza-Avella, R. López, F. Martinez-Ortega, E.A. Páez-Mozo, R. Gómez, J. Nano Res. 5 (2009) 95–104.
[53] Y. Di Iorio, E. San Roman, M. Litter, M. Grela, J. Phys. Chem. C 112 (2008) 16532–16538.
[54] E. Chamarro, A. Marco, S. Esplugas, Water Res. 35 (4) (2001) 1047–1051.
[55] J. Scott, D. Ollis, Environ. Prog. 14 (2) (1995) 88–103.
[56] F. Al-Momani, J. Degorce-Dumas, J. Roussy, O. Thomas, J. Photochem. Photobiol. A 153 (2002) 191–197.
[57] V. Elías, E. Sabre, E. Winkler, M. Satuf, E. Rodriguez-Castellón, S. Casuscelli, G. Eimer, Microporous Mesoporous Mater. 163 (2012) 85–95.